Analysis of shock oscillations of an external compression supersonic inlet through unsteady numerical simulations

Pierre Grenson, Samir Beneddine

Analysis of shock oscillations of an external compression supersonic inlet through unsteady numerical simulations

P. Grenson* and S. Beneddine†
DAAA, Onera, The French Aerospace Lab, 8 rue des Vertugadins, 92190 Meudon, France

In this study, the ability of unsteady numerical simulations to predict the flow behavior in an external compression supersonic inlet has been investigated. The attention has been focused on the dynamical characteristic of the flow as the ingested mass-flow is progressively reduced from supercritical condition to the subcritical flow regime that features large oscillations of the shock system. This analysis is based on experimental data gathered on a rectangular inlet at $M = 1.8$. Numerical simulations have been performed on simplified model of a reduced size and Reynolds number in order to make it tractable for high-fidelity simulations. In the present paper, results are presented for (U)RANS and hybrid RANS-LES simulations. It is shown that URANS is unable to predict the flow oscillations which occur before the big buzz whereas hybrid RANS-LES are able to predict the flow spectra in fair agreement with the experimental data. The unsteady data computed through ZDES of one particular configuration is then employed to highlight the pressure mode associated with the little buzz phenomenon. It is shown that it features a more complicated shape than the fundamental open-closed duct pressure mode, which has generally been used to estimate buzz frequency. Eventually ZDES results are compared to a stability analysis based on a steady RANS field.

Nomenclature

Acronyms

(U)RANS	(Unsteady) Reynolds Averaged Navier-Stokes
AIP	Aerodynamic Interface Plane
CFL	Courant-Friedrichs-Lewy number
DDES	Delayed Detached Eddy Simulation
LES	Large Eddy Simulation
PIV	Particle Image Velocimetry
PSD	Power Spectrum Density
SA	Spalart-Allmaras
SWBLI	Shock Wave Boundary Layer Interaction
TR	Throttling ratio
ZDES	Zonal Detached Eddy Simulation

Greek Symbols

δ	Boundary layer thickness [m]
δ_ω	Vorticity thickness [m]
η	Efficiency [-]
γ	Adiabatic constant [-]
ν	Kinematic viscosity [m^2s^{-1}]
ρ	Density [kgm^{-3}]
Σ	Critical section ratio [-]
σ	Mode growth rate [-]
τ_c	Buzz characteristic time [s]
ε	Normalized flow ratio [-]

Roman Symbols

A	Cross section area [m^2]
c	Speed of sound [ms^{-1}]
f	Frequency [Hz]
H	Inlet height [m]
h_t	Throat height [m]
L	Pipe length [m]
M	Mach number [-]
p_i	Stagnation pressure [Pa]
p_s	Static pressure [Pa]
q_m	Mass flow [kg/s]
T	Temperature [K]
u	Flow velocity [ms^{-1}]
u_τ	Friction velocity [ms^{-1}]
x, y, z	Cartesian coordinates [m]
X_{ob}	Plug axial position [mm]

Subscripts

$.^+$	Wall unit
$\cdot_0$	Free-stream condition

*PhD, Research Scientist, pierre.grenson@onera.fr
†PhD, Research Scientist, samir.beneddine@onera.fr

I. Introduction

The role of supersonic air inlets is to decelerate the incoming supersonic air to a low subsonic flow. This operation must induce the minimum possible total pressure losses while ensuring a stable flow regime. As the amount of air required by the engine decreases below a certain threshold, the shock system ahead of the air intake may however suffer from large oscillations. This phenomenon, referred to as buzz, is highly undesirable as it can strongly alter the engine thrust (combustion extinguishment) or lead to unacceptable structural loads. Prediction of the flow stability characteristics of an air inlet at different operating conditions is therefore a critical issue and is the major concern of the present work.

Numerous studies have addressed these self-excited flow oscillations, with different explanations about their onset. According to the experiments of Ferri and Nucci [1] on cylindrical supersonic inlet, the buzz is initiated when the vortex sheet due to the intersection between the oblique and normal shock passes below the cowl lower surface, which causes flow separation. Another explanation is due to Dailey [2] who associates buzz with the flow separation on the compression surface that originates from the shock-boundary layer interaction (SBLWI). In both cases, the separation chokes the flow at the intake throat which eventually triggers the buzz.

Fisher *et al.* [3] observed on a rectangular inlet that when the mass flow is decreased, small-amplitude oscillations first occur. This regime was then referred to as little buzz. With further reduction of the mass flow rate, larger amplitude oscillations take place, which corresponds to the big buzz. The frequency of the little and big buzz were found to be similar. The existence of two buzz regimes was also reported by Trapier *et al.* [4] on a rectangular mixed compression inlet. They observed the big buzz frequency to be one order of magnitude lower than the little buzz frequency. Following the idea of Newsome [5], the little buzz frequency was related to the first harmonic of the resonance modes of the inlet duct. As shown by Soltani and Spahi-Younsi [6], the little buzz emergence could depend on the free-stream conditions.

Several authors have attempted to study inlet buzz numerically. Different work [5, 7–9] showed that unsteady RANS (URANS) simulations succeeded in reproducing inlet buzz, with a fair prediction of the phenomenon frequency. Due to high flow Reynolds number encountered in air inlet configurations, which severely increases the required mesh size, there have been so far few attemps of numerical simulations using high-fidelity approaches such as LES or hybrid RANS-LES. Trapier *et al.* [10] investigated the use of DDES (Delayed Detached Eddy Simulation) for simulating their experimental configuration. This approach not only permitted to retrieve the salient features of the big buzz but also allowed for a deeper understanding of the flow field behavior. Lyubimov and Poteknia [11] have recently applied hybrid RANS-LES simulation on the Trapier's configuration for various flow regimes, with and without bleed system. A fair qualitative prediction of the pressure fluctuations for different throttling ratio is reported, but the limited number of points in the computational mesh restricts the scope of these results. In the aforementioned studies, no attempt in simulating the flow regime at which little buzz takes place has been reported. The most advanced study dedicated to hybrid RANS-LES simulation of little buzz is due to Candon et *al.* [12]. Those author focused on a low-boom cylindrical external compression inlet for which shock oscillations have been seen to take place for a mass flow ratio close to the design configuration. Through an analysis of the time lag between unsteady pressure signals widespread across the streamwise direction of the duct, they related the shock oscillation to upstream-running compression waves from the diffuser that moved at acoustic speed. This study was however restricted to a unique mass flow ratio and the simulation duration was too short to bring conclusive results about the phenomenon frequency. It would then be interesting to assess the evolution of the shock oscillation frequency as the mass flow ratio is reduced.

Hence, the goal of the present study consists in evaluating the ability of both URANS and hybrid RANS-LES simulation strategies to reproduce flow oscillations in supersonic air inlets when the mass flow ratio is progressively decreased. The methodology is validated against an experimental data gathered on an external compression rectangular inlet. The chosen configuration exhibits the originality that the entry plane is preceded by a flat pate on which a turbulent boundary layer develops. The paper is organized as follows. The experimental setup and associated results are presented in Sec. II. Sec. III is devoted to the simulation parameters that have been selected. Comparison of the numerical data to the experiments is carried out in Sec. IV. In Sec. V, the pressure fluctuations of a little-buzzed configuration are thoroughly analyzed. Finally, a stability analysis in conducted in Sec. VI.

II. Experimental Data

A. Experimental setup

The experiment was performed in the Onera S3MA supersonic wind tunnel. It is a blow-down wind tunnel with a rectangular test section (0.86×0.70 m). The experimental model is sketched in Fig. 1. It consists of a rectangular duct

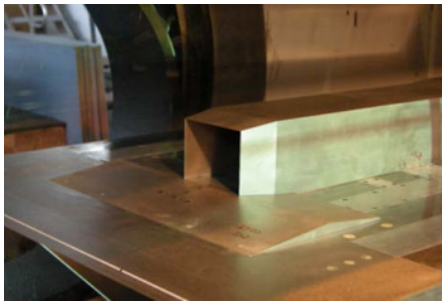

(a) Photography.

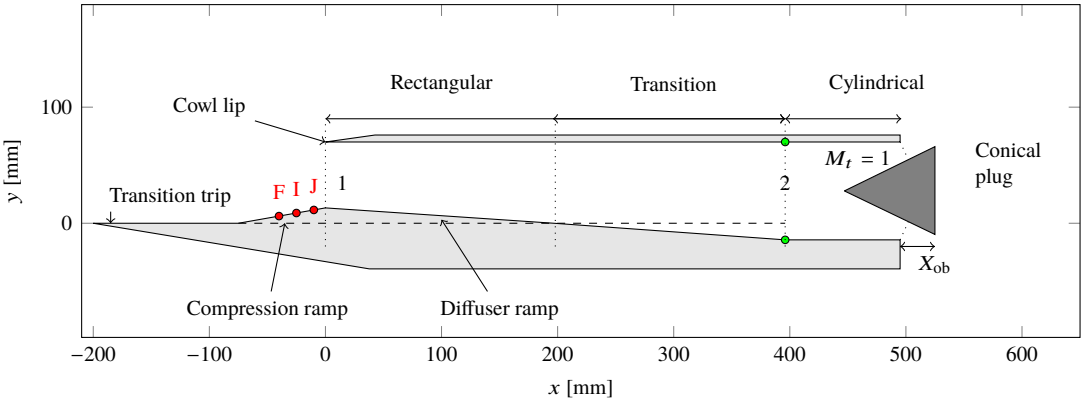

(b) Oxy plane.

Figure 1 Experimental setup. (Green circles) Static pressure taps. (Red circles) Kulite transducers.

of capture area $A_1 = 70\,\text{mm} \times 80\,\text{mm}$ preceded by a 10°-compression ramp and a 125 mm-long flat plate. The mass flow rate q_m through the air inlet is fixed by the relative position of a conical plug X_{ob} into the cylindrical duct section of diameter $D = 84.4\,\text{mm}$, of equivalent area to A_1. The transition between the 200 mm long rectangular section and the 100 mm long cylindrical one is progressively achieved over a length of 200 mm. The diffuser ramp downstream of the inlet section has a angle of 4°. The $M = 1.8$ developing boundary layer on the upstream plate is artificially tripped by means of a roughness band (CADCUT) located 15 mm downstream of the leading edge. The upstream stagnation pressure $p_{i,0}$ is 171415 Pa and the stagnation temperature $T_{i,0}$ is 310 K.

The model is equipped with static pressure taps in section 2 (green dots in Fig. 1) in order to measure the inlet performance. Additionally, unsteady pressure transducers (Kulites) are located on the compression ramp. As they lie in the neighborhood of the shock foot, they will give valuable information about the shock oscillation. Windows on the side wall of the wind tunnel allowed for both Schlieren pictures (25 im/s) and PIV measurements of the flow on the flat plate and compression ramp.

B. Results

1. Characteristic curve

Performance of an air inlet are generally given through the characteristic curve which expresses the pressure recovery at the engine entry plane (also called AIP, for Aerodynamic Interface Plane) as a function of the mass flow ratio. In the experiments, this plane corresponds to section 2 in Fig. 1, located ahead of the conical plug. The pressure recovery, also called efficiency η, is defined as:

$$\eta = \frac{p_{i,2}}{p_{i,0}} \tag{1}$$

The upstream stagnation pressure $p_{i,0}$ is given by the static pressure in the wind tunnel air tank. Measurement of the mean stagnation pressure in the AIP would ideally require a pressure rake. As such a device was not used in the present study, the stagnation pressure $p_{i,2}$ is computed from the static wall pressure p_2 and the geometrical section ratio A_t/A_2

between the AIP and the sonic throat. This method relies on the hypothesis that the flow is isentropic between section 2 and the throat, which is a fair hypothesis if no shock is present in-between:

$$p_{i,2} = p_{s,2}\left(1 + \frac{\gamma - 1}{2}M_2^2\right)^{\frac{\gamma}{\gamma-1}} \quad \text{with} \quad M_2 = \Sigma^{-1}\left(\frac{A_t\left(X_{\text{ob}}\right)}{A_2}\right) \tag{2}$$

The mass flow through section 2 $q_{m,2}$ is conventionally normalized by the theoretical maximal mass flow ratio that can be ingested by the inlet $q_{m,\max}$:

$$\varepsilon = \frac{q_{m,2}}{q_{m,\max}} \tag{3}$$

In the case of an external compression inlet with "shock-on-lip" oblique shocks, $q_{m,\max}$ can be expressed as:

$$q_{m,\max} = 0.04042\frac{p_{i,0}A_1}{\Sigma\left(M_0\right)\sqrt{T_{i,0}}} \tag{4}$$

with $T_{i,0}$ the upstream stagnation temperature, which is considered constant throughout the flow. By means of Eqs. (1) and (2), the normalized mass flow ratio can be rewritten as:

$$\varepsilon = \eta\frac{A_t\left(X_{\text{ob}}\right)}{A_1}\Sigma\left(M_0\right) \tag{5}$$

with the throat section A_t depending on the plug position X_{ob}. The throttling ratio is defined as the ratio between the critical section A_t and the fully open duct end section A_{exit} and quantify the blocking degree of the air inlet.

The characteristic curve obtained from the experimental measurements is plotted in Fig. 2. Schlieren vizualisation and PIV mean velocity fields for various throttling ratios are also represented as they allow for the characterization of the shock pattern on the compression ramp. From the spectral results that will be presented in the next section, the dynamical feature of the shock system is also indicated (big buzz, little buzz or stable flow). Fig. 2 shows that, as the throttling ratio is incrementally reduced, three flow regimes successively take place. For high throttling ratio (TR = 0.74), only the oblique shock generated by the compression ramp is visible on the Schlieren visualization. At this condition the flow is supercritical *i.e.* the terminal normal shock that slows the flow from supersonic upstream condition down to subsonic condition at the AIP is located inside the duct. Because the supersonic flow is accelerated in the diffuser, the normal shock upstream Mach number is high, what induces strong stagnation pressure losses. At TR = 0.70, the normal shock lies right at the inlet section so that the flow is subsonic across the entire duct. This operational point constitutes the design point for which the pressure recovery is the highest ($\eta = 0.83$). As the mass flow ratio is reduced, the normal shock moves upstream. The shock system exhibits a classical λ-structure owing to the interaction with the boundary layer generating a separation region. In this regime, the shock system has been shown to suffer from slight oscillations that can be associated to little buzz. Below a certain throttling ratio (between TR = 0.60 and TR = 0.56), these shocks oscillations are strongly amplified, meaning that the air inlet is in the big buzz flow regime. In this regime, the flow separation occurs ahead of the compression ramp which explains the strong degradation of the pressure recovery.

2. Power Spectral Density

Flow unsteadiness is experimentally characterized by the power spectral density (PSD) of static pressure signals gathered by the three Kulites transducers located on the compression ramp and reported in Fig. 3. It is shown that no shock oscillation is observed for the highest throttling ratio TR = 0.74. For the design condition (TR = 0.70), the PSD of the nearest probe to the inlet section exhibits a peak at frequency $f = 107$ Hz. As the throttling ratio is further decreased, this peak emerges for the more upstream probes, depending on the shock location:

- at probe J for TR = 0.67;
- at probe J and F for TR = 0.65 and TR = 0.60.

The fact that the frequency peak appears only on certain probes indicates that the shock oscillations remain localized near the mean shock location which is the main feature of the little buzz regime.

For the lowest throttling ratio (TR = 0.56), the three probes exhibit a peak of high energy content at the frequency $f = 83$ Hz.This shows that the shock oscillation has a strong amplitude and spans the entire compression ramp. This constitutes the spectral manifestation of the big buzz.

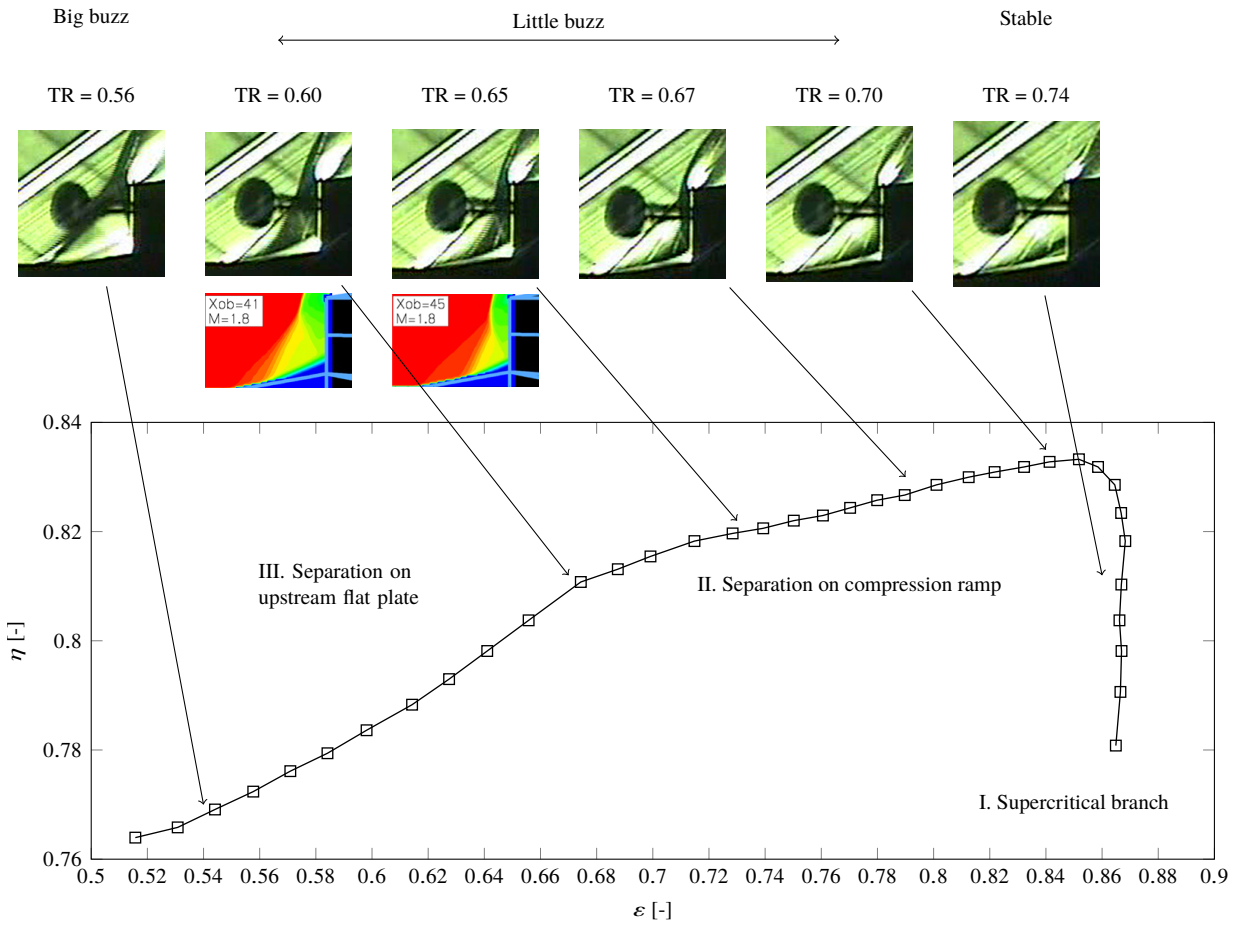

Figure 2 Different flow regimes as the conical plug progresses into the inlet duct (decreasing throttling ratio TR). (Top) Schlieren visualization. (Middle) Mean velocity field from PIV. (Bottom) Characteristic curve $\eta - \varepsilon$.

Following the idea of Newsome [5], we tried to relate the observed frequencies of $f = 107\,\text{Hz}$ (little buzz) and $f = 83\,\text{Hz}$ (big buzz) to those of the acoustic modes ($n = 0, 1, 2\ldots$) of an open-closed duct whose frequency is given by the following formula:

$$f_n = (2n+1)\,\frac{c}{4L}\left(1 - M^2\right) \tag{6}$$

where M is the mean Mach number and $c = \sqrt{\gamma \mathcal{R} T}$ is the mean speed of sound in the duct. The throat side is generally considered as acoustically "closed" because the velocity at the throat is constant, provided that the throat is choked ($M = 1$). Formula (6) assumes a uniform distribution of both M and c in the duct, which is not really the case in the presence of a diffuser through which flow is decelerated. For TR = 0.75, we consider the mean Mach number and the static temperature to be that measured in section 2: $M = M_2 = 0.5$ and $T_{s,2} = T_{i,0}\left(1 + \frac{\gamma-1}{2} M_2^2\right)^{-1} = 295\,\text{K}$, which gives $c = 344\,\text{m/s}$. The acoustic length L is the distance between the inlet section 1 and the throat section t, *i.e.* $L = 0.5\,\text{m}$. With these values the fundamental frequency $f_{n=0}$ of the open-closed duct is 129 Hz. Considering the hypotheses made in Eq. (6), this frequency is fairly close to that observed for TR between 0.60 and 0.70 and which is related to the little buzz phenomenon.

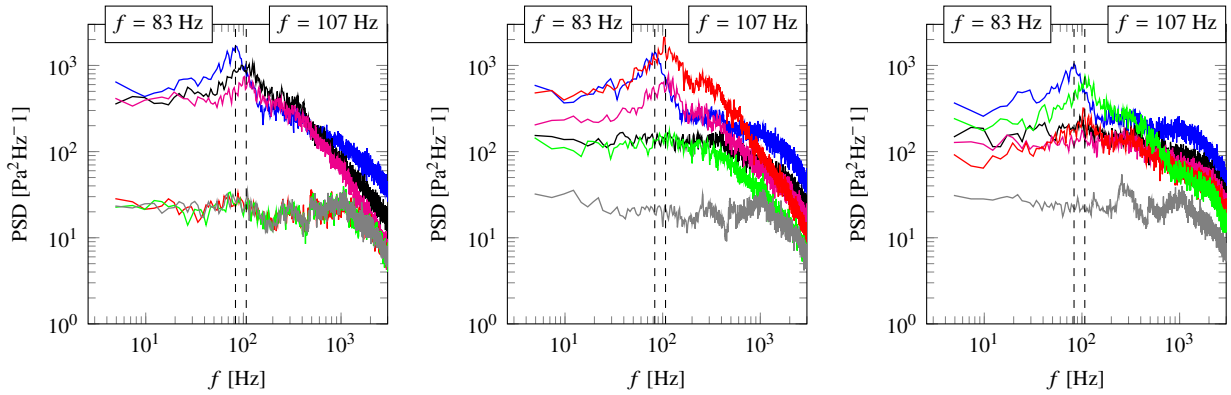

(a) Probe F. (b) Probe J. (c) Probe I.

Figure 3 Power spectral density of the static pressure signal measured at three probes on the compression surface. (——) TR = 0.56. (——) TR = 0.60. (——) TR = 0.65. (——) TR = 0.67. (——) TR = 0.70. (——) TR = 0.74.

Parameter	Experimental setup	Reduced model
$T_{i,0}$	310 K	310 K
M_0	1.8	1.8
$p_{i,0}$	171 415 Pa	300 000 Pa
H	70 mm	10 mm
δ/H	4.1%	5.1%
Re_{δ_2}	4000	1300
Buzz frequencies (big and little)	83 Hz and 107 Hz	581 Hz and 750 Hz
Δt	0.2 μs	0.1 μs
Time steps (20 buzz cycles)	1 250 000	360 000
Mesh size (LES)	1500 M	125 M

Table 1 Computational reduced model parameters compared to the experimental ones.

III. Simulation Parameters

A. Computational setup

Performing high-fidelity simulations such as hybrid RANS-LES or LES on the experimental configuration described hereabove would require a large number of both mesh cells, due to the high Reynolds number, and time steps because of the low-frequency of the buzz phenomenon. For these reasons a reduced computational configuration has been selected for the present study. The chosen parameters are compared to the experimental ones in Tab. 1. As the buzz phenomenon is expected to be related to the SWLBI ahead of the inlet section, they have been determined so that the shock system and the relative thickness δ/H of the boundary layer on the compression ramp are similar to the experiments. The overall geometry has been scaled by a factor $1/7$ in order to increase by the same factor the buzz frequency, which eventually allows to reduce the number of time step required to span a given number of buzz cycles. The freestream stagnation pressure has been raised to 300 000 Pa so that the boundary layer can still maintain turbulent. Finally, side walls have been omitted so that the z direction is considered as homogeneous (Fig. 4). Contrary to the experimental configuration, the duct section is therefore rectangular everywhere. This explains why the diffuser ramp is followed by an horizontal surface up to the sonic throat, located at the same distance from the inlet section as the plug in the experiments.

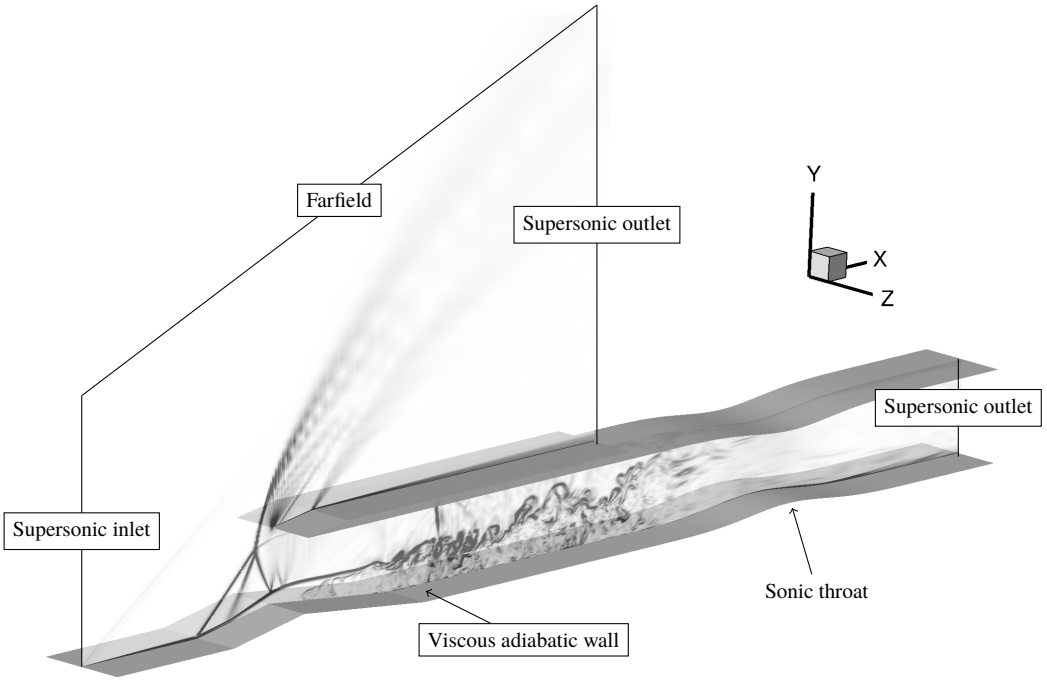

Figure 4 Computational setup: boundary conditions and sonic throat for mass flow regulation. The instantaneous field of density gradient magnitude $[\![\nabla\rho]\!]$ from ZDES simulation is represented in Oxy plane.

B. Numerical parameters and modeling

Computations have been performed using the Navier-Stokes structured multi-block solver FastS [13], developed at Onera. (U)RANS simulations have been conducted with both the Spalart-Allmaras (SA) [14] turbulence model which solves a unique transport equation for the eddy viscosity $\tilde{\nu}$ and a variant (SAc) [15] which improves the behavior in compressible mixing layers. The Zonal Detached Eddy Simulation (ZDES) [16] has been selected as the hybrid RANS-LES approach to conduct high-fidelity simulation. This strategy has been proven accurate for prediction of different configuration of both free [17] and wall bounded flows [18]. As for the SA model, a transport equation for $\tilde{\nu}$ is solved. The destruction term in this equation is modified depending on the mesh grid size Δ and the wall distance d_w so that the RANS model switches to an LES subgrid-scale one in the detached flows. A protection function f_d, based the flow local properties, enforces RANS mode in attached boundary layer.

The $20.7M$-cells mesh is represented in Fig. 5a. The cell dimensions Δ in the three cartesian directions have been determined to fullfill the requirements of both:

- LES in the shear layer, expressed in vorticity thickness $\delta_\omega = \frac{(u_{\max}-u_{\min})}{\partial u/\partial y_{\max}}$ unit:

$$\Delta x = \delta_\omega/2, \quad \Delta y = \delta_\omega/15 \quad \text{and} \quad \Delta z = \delta_\omega/3 \tag{7}$$

- ZDES for the boundary layers above the viscous walls, expressed in wall unit $(\cdot)^+ = (\cdot)\,u_\tau/\nu$:

$$\Delta x^+ = 100, \quad \Delta y^+ = 1 \quad \text{and} \quad \Delta z^+ = 100 \tag{8}$$

Fig. 5c shows the flow regions treated in RANS and LES at a particular time step. It is seen that attached boundary layers on both the lower wall (compression and diffuser ramp) and the inlet cowl correspond to RANS region while the rest of the inlet is in LES mode.

The same grid has been used for (U)RANS and ZDES simulations. Spatial discretization is realized by the AUSM+P numerical scheme [19]. The time integration is carried out by means of the second-order-accurate backward scheme of Gear. Time step $\Delta t = 1.0 \times 10^{-7}$ s has been chosen so that the *convective* CFL number, defined as:

$$\text{CFL} = \frac{\sqrt{u_x^2 + u_y^2 + u_z^2}\,\Delta t}{\min(\Delta x, \Delta y, \Delta z)} \tag{9}$$

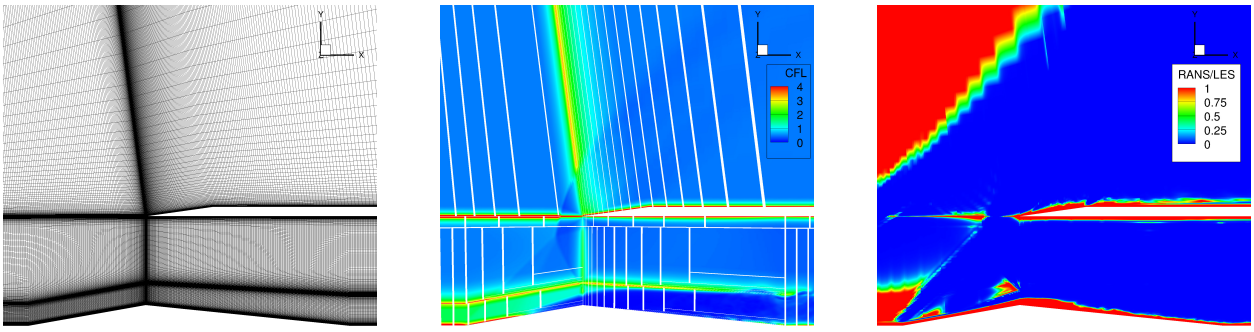

(a) Mesh distribution.

(b) Convective CFL distribution.

(c) RANS and LES regions (RANS =1, LES = 0).

Figure 5 Numerical parameters.

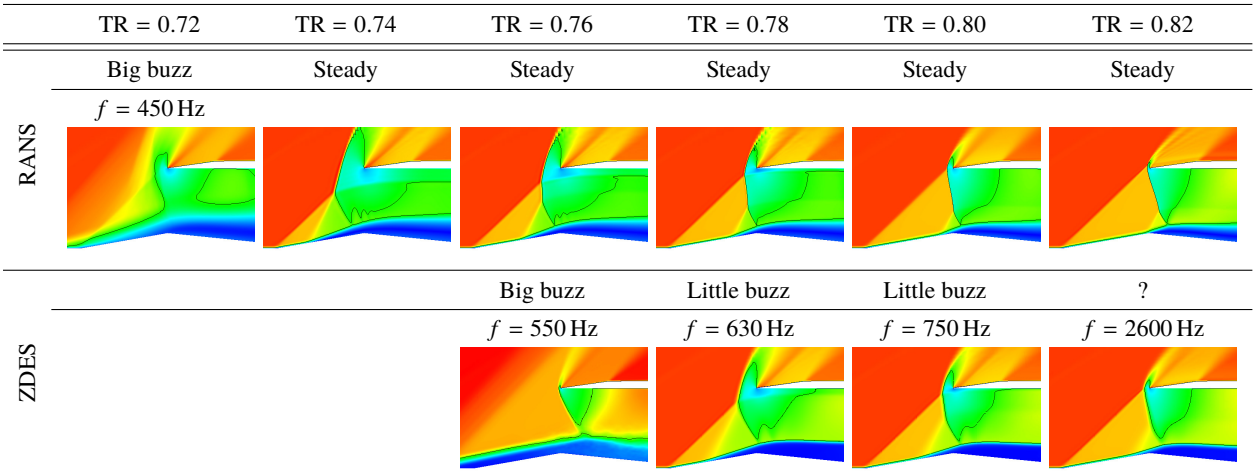

Figure 6 Mean Mach number M (blue: $M = 0$, red: $M = 1.94$) in the vicinity of the inlet section for different throttling ratio TR. The dominant frequency f observed in each configuration is also reported. (Top) URANS with SAc. (Bottom) ZDES.

remains everywhere less than 5 (Fig. 5b).

For the URANS simulations, the flow has been initialized with the throat section completely open *i.e.* the throttling ratio TR is 1.0 (see inset (a) in Fig. 7). At $t = 0$, the throat is suddenly closed to a given TR and the flow evolution is computed with a global time-stepping. For the ZDES simulations, the flow has been initialized with the URANS solution for the corresponding throttling ratio. Statistics are gathered after the transient has been evacuated. Depending on the throttling ratio the simulation duration spanned between 8 (for TR = 0.76) to 40 (for TR = 0.78) characteristic times τ_c based on the expected shock oscillation frequency. Computations have been performed on the NEC cluster of Onera (SATOR). Calculation domain has been split in 297 blocks, balanced onto 280 Intel Xeon « Broadwell » E5-2680v4 processors. Effective CPU cost per iteration per cell was 0.7 μs.

IV. Comparison against experimental results

A. Mean flow features

The mean flow obtained for decreasing throttling ratio from TR = 0.82 to 0.72 by means of both RANS and ZDES simulations are gathered in Fig. 6.

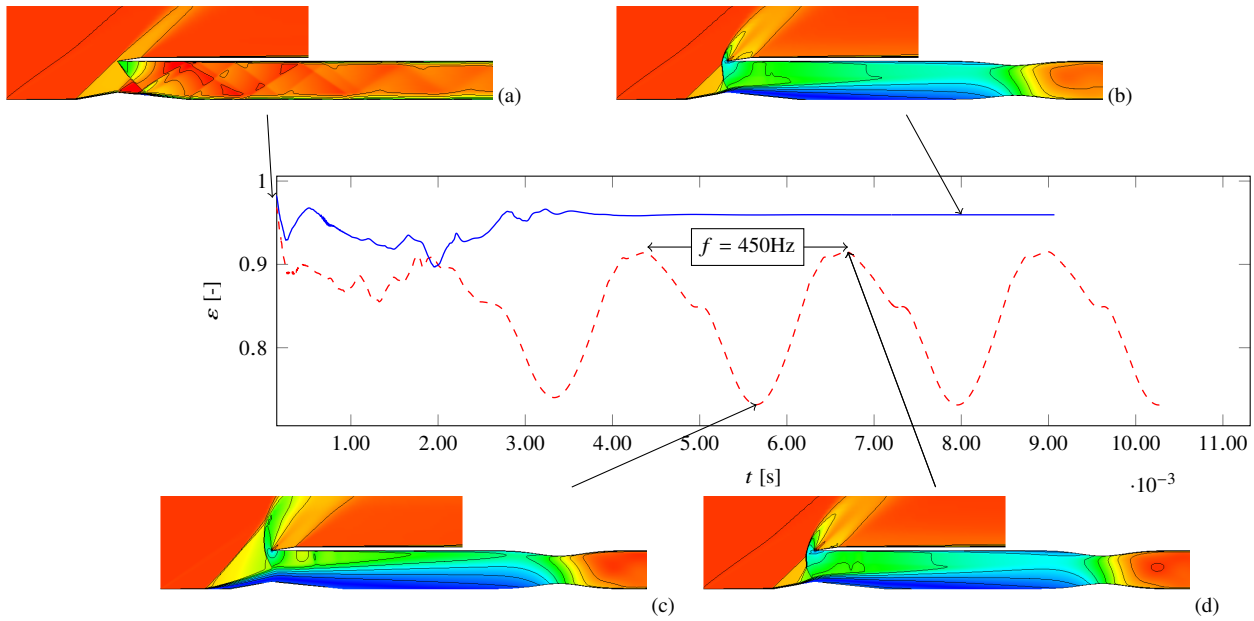

Figure 7 Time-evolution of the air inlet mass flow ratio with URANS simulations. (——) TR = 0.78. (- - -) TR = 0.72. Insets correspond to instantaneous Mach number field (colormap from $M = 0.0$ to 1.9). (a) Initial field for URANS calculations. (b) Steady solution for TR = 0.78. Solution field corresponding to (c) the lowest and (b) highest value of ε during a buzz cycle.

1. URANS

It can been seen that, for decreasing TR, the shock system progresses upstream along the compression ramp as observed in the experiments (Fig. 2). By inspection of the shock system position, one can associate the numerical throttling ratio to the experimental one. The computational case at TR = 0.76 can for example be associated with the experimental configuration at TR = 0.65. The fact that the same shock system pattern are observed for a higher throttling ratio in the simulation originates from the absence of the side walls in the computational domain. Contrary to the experiments there is no lateral spillage.

For the URANS simulation an indication of flow unsteadiness is also reported in Fig. 6. *Steady* means that the URANS field converges towards a stationary solution. It should first be noticed that all the URANS computation above TR = 0.74 converges to a stationary solution despite the intense transient due to the throat closure and the global time-stepping, as illustrated in Fig. 7 for TR = 0.78. Self-excited oscillations only appear for TR below 0.74, as also shown in Fig. 7. The frequency of these oscillations is 450 Hz which corresponds approximately to the expected value of the buzz phenomenon on the reduced computational model ($f = 581$ Hz). These results seem to indicate that URANS is able to reproduce the big buzz but fails to predict any fluctuations for TR which are expected to exhibit little buzz.

2. ZDES

As observed in Fig. 6, the shock system pattern obtained with the ZDES simulation seems to be shifted towards upstream position compared to URANS for the same throttling ratio. For instance, the flow field of TR = 0.80 with ZDES compares well to that of URANS with TR = 0.78. In Fig. 6 an indication about the unsteady behavior of the flow, that will be discussed in more detail in Sec. C, is also reported. It turns out that, as a consequence of the shift in TR between URANS and ZDES, the big buzz occurs for higher throttling ratio for ZDES.

B. Characteristic curve

Characteristic curves $\varepsilon - \eta$ obtained with both RANS and ZDES simulations are reported in Fig. 8 and compared to

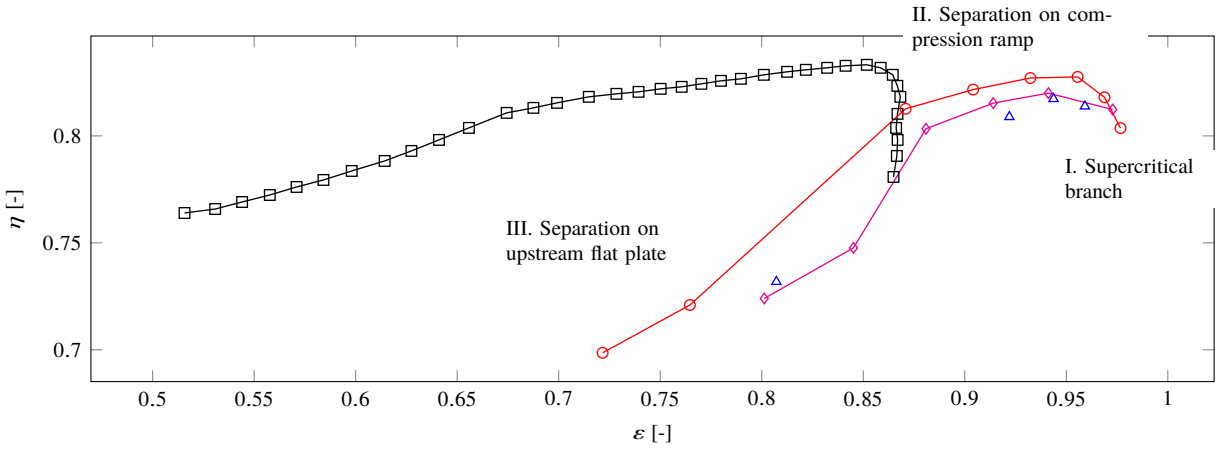

Figure 8 Comparison of characteristic curves from numerical simulations to experimental data. (▫▫▫) Experiments. (△△△) ZDES. (○○○) RANS SA. (◇◇◇) RANS SAc.

the experiments. It should be mentioned that η and ε are computed by means of integrals over the plane A_2:

$$\eta = \frac{\frac{1}{A_2}\int_{A_2} p_i(x,y,z)\mathrm{d}A}{p_{i,0}} \tag{10}$$

$$\varepsilon = \frac{\int_{A_2} \rho u_x(x,y,z)\mathrm{d}A}{q_{m,\max.}} \tag{11}$$

These definitions are more accurate than their experimental counterparts (Eqs. (1) and (5)) since they do not suffer from the flow isentropy hypothesis and an isolated pressure measurement.

It is seen in Fig. 8 that the mass flow ratio predicted by the numerical simulations is shifted towards $\varepsilon = 1$. This discrepancy with respect to the experiments is easily explained by the absence of the side walls in the computational domain that reduces the lateral spillage. The maximum efficiency at the critical point ($\eta \simeq 0.8$) is remarkably reproduced by the simulations although the computational domain is different from the experimental setup in both size and Reynolds number. The three regimes discussed in Sec. II and labeled in Fig. 2 can be fairly distinguished on the RANS simulations. It is seen that the three ZDES simulations with the highest mass flow ratio (TR = 0.82, TR = 0.80 and TR = 0.78) belong to the stable subcritical branch (II) while the lowest mass flow ratio (TR = 0.76) lies in the buzzed subcritical branch (III).

C. Unsteady flow features

A representative instantaneous field of the density gradient magnitude $[\![\nabla\rho]\!]$ in the longitudinal plane Oxy obtained from ZDES (TR = 0.78) is represented in Fig. 4. It turns out that the resolved small-scale turbulent structures appears downstream of the diffuser ramp due to the shear layer between the high speed central flow and the separated region behind the diffuser. These structures are advected towards the sonic throat where they disappear due to the favorable pressure gradient and the mesh coarsening. There is no fine turbulent structures in the vicinity of the shock-boundary layer intersection which is, for the most part, treated in RANS (Fig. 5c).

Because we are interested in the ZDES ability to retrieve buzz features, the power spectral density of the pressure signal at probes F, I and J located on the compression ramp (Fig. 1) is plotted in Fig. 9 for the different throttling ratios. It is shown that the PSDs exhibit several peaks whose frequency is not the same depending on the throttling ratio. For TR = 0.82 down to TR = 0.78, pressure signals have both low frequency peaks, which are highlighted on the left plots in Fig. 9, and several high frequency peaks. Those high-frequency peaks are multiple of the frequency $f = 12.5$ kHz. The low frequency of TR = 0.80 and TR = 0.78, respectively $f = 750$ Hz and $f = 630$ Hz, are not far off the expected frequency of the little buzz on the reduced model ($f = 749$ Hz) which is related to the fundamental acoustic mode ($n = 0$) of the duct. For the higher throttling ratio TR = 0.82, the lowest frequency is almost four times higher and does

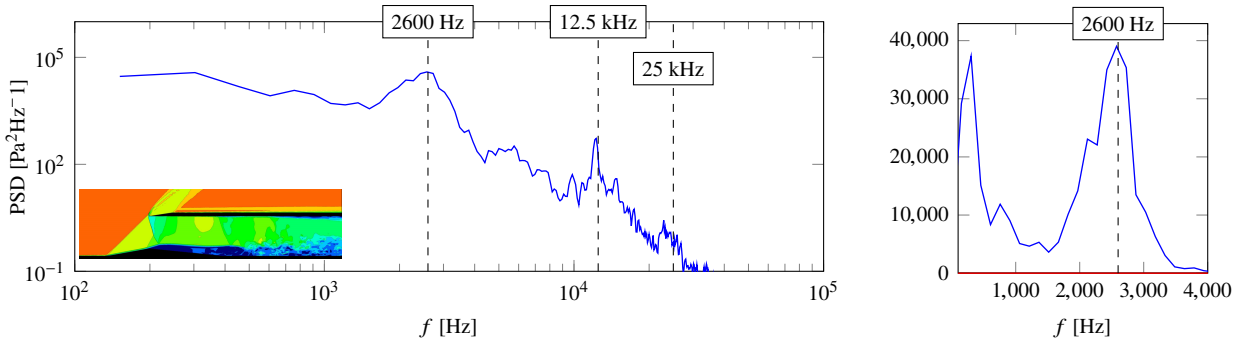

(a) TR = 0.82. Δf = 151.5 Hz

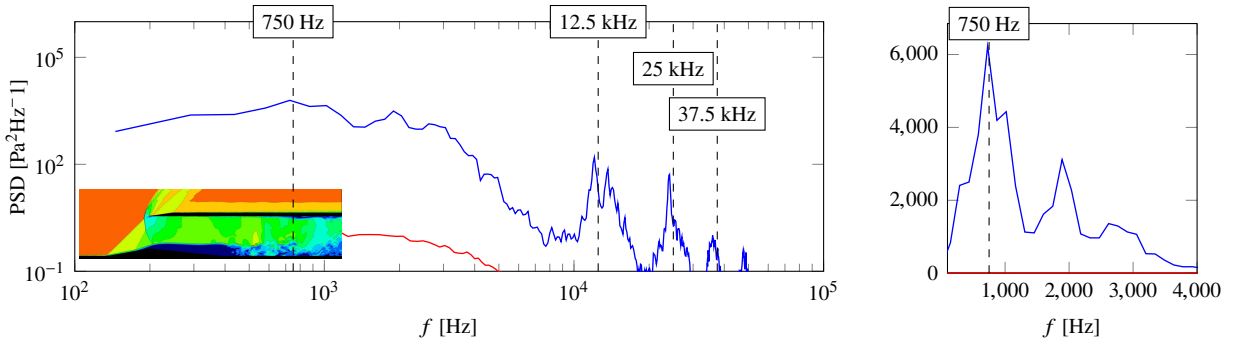

(b) TR = 0.80.Δf = 145.5 Hz

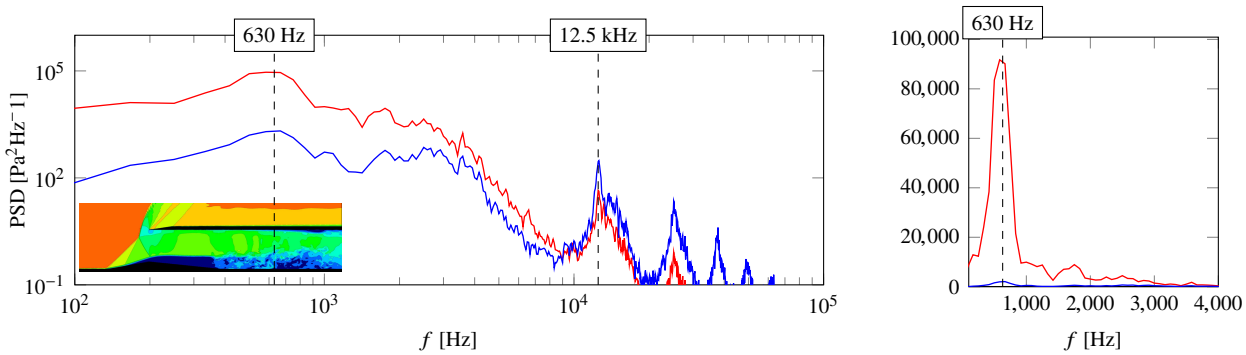

(c) TR = 0.78. Δf = 83.3 Hz

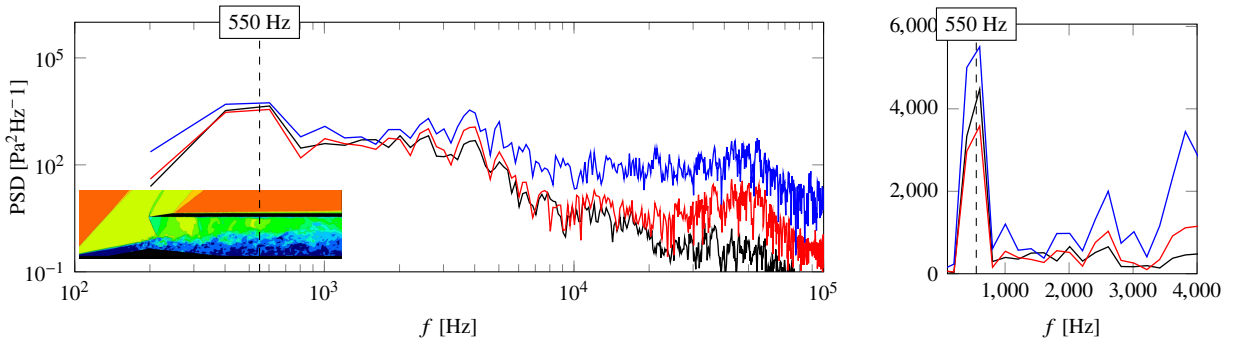

(d) TR = 0.76. Δf = 200.9 Hz

Figure 9 Power spectral density of unsteady static pressure for three probes on the compression ramp obtained with ZDES for decreasing throttling ratio. (Left) Logarithmic plot. (Right) Linear plot in the low frequency range. (——) Probe K. (——) Probe I. (——) Probe J. Probe location is depicted in Fig. 1. (Inset in lower left corner) Instantaneous Mach number distribution in $z = 0.005$ plane.

	M	a	$f_{n=0}$	f_{ZDES}	$f_{exp.}$
TR = 0.82	0.76	328 m/s	468 Hz	2600 Hz	
TR = 0.80	0.72	329 m/s	534 Hz	750 Hz	7×107 Hz = 749 Hz
TR = 0.78	0.69	331 m/s	581 Hz	630 Hz	
TR = 0.76	0.67	331 m/s	616 Hz	550 Hz	7×83 Hz = 581 Hz

Table 2 Comparison of the observed peak frequency to that of the fundamental acoustic mode $n = 0$ computed from Eq. (6) for different throttling ratio.

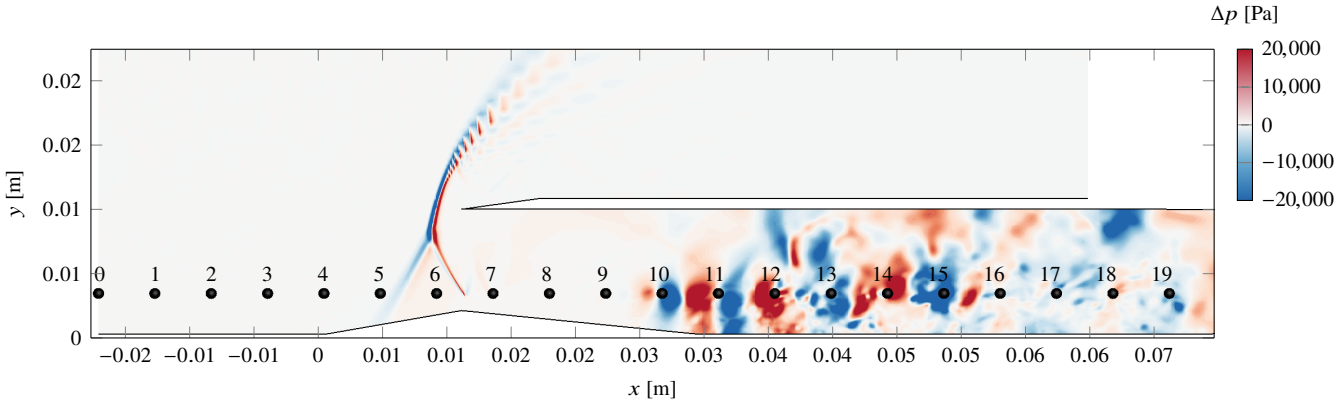

Figure 10 Instantaneous field of the fluctuating pressure $\Delta p = p - \overline{p}$ in the $z = 0.005$ plane. (Black spheres) Probe number and location along the air inlet.

not correspond to any frequency observed in the experiments. One can suppose that the $n = 4$ acoustic mode is excited in that case, even though the frequency is not exactly equal to 750 Hz $\times$ 4 = 3000 Hz.

As it was observed in the experiment (Fig. 3), the frequency peaks emerge on different probe depending on the throttling ratio and the related mean shock position. This is not the case for TR = 0.76 for which the three pressure probes experience the shock oscillations, corresponding to the phenomenology of the big buzz. The peak frequency is $f = 550$ Hz that is close to the expected big buzz frequency of $f = 581$ Hz. Thus the ZDES simulations have been able to reproduce the change in the frequency peak between little and big buzz.

Contrary to the experiments, the numerical simulation gives access to the mean flow properties in the duct. This allows to compute the fundamental acoustic mode of the duct from Eq. (6) by using the computed value of both the Mach number M and speed of sound c in the duct. In Tab. 2, the calculated fundamental frequency of the duct acoustic mode is compared to the dominant one observed for ZDES simulations and the expected frequency from the measurements. For TR = 0.78, this frequency is close to that evidenced in the ZDES simulation. The mean Mach number in the duct decreases with the throttling ratio whereas the speed of sound maintains a nearly constant value. Consequently, the acoustic frequency tends to increase with the throttling ratio, which is in opposition to what is observed both in the ZDES simulations and experimentally. This indicates that the buzz frequency cannot be simply estimated by the fundamental acoustic mode frequency of a one-dimensional open-closed duct. To get more insight on the unsteady flow features highlighted by ZDES simulations, the following section will address the spatial structure of the mode corresponding to the pressure fluctuations at the dominant frequency.

V. Detailed analysis of pressure fluctuations for TR = 0.78

In this section, we focus on the TR = 0.78 case which has been shown to exhibit little buzz at a frequency of 630 Hz. In the following, the aim is to characterize the spatial organization of the pressure fluctuations in the air inlet. For that purpose, the pressure signal from the ZDES simulation has been recorded by 20 probes widespread along the longitudinal axis of the air inlet. Fig.10 shows their location along with the instantaneous field of the pressure

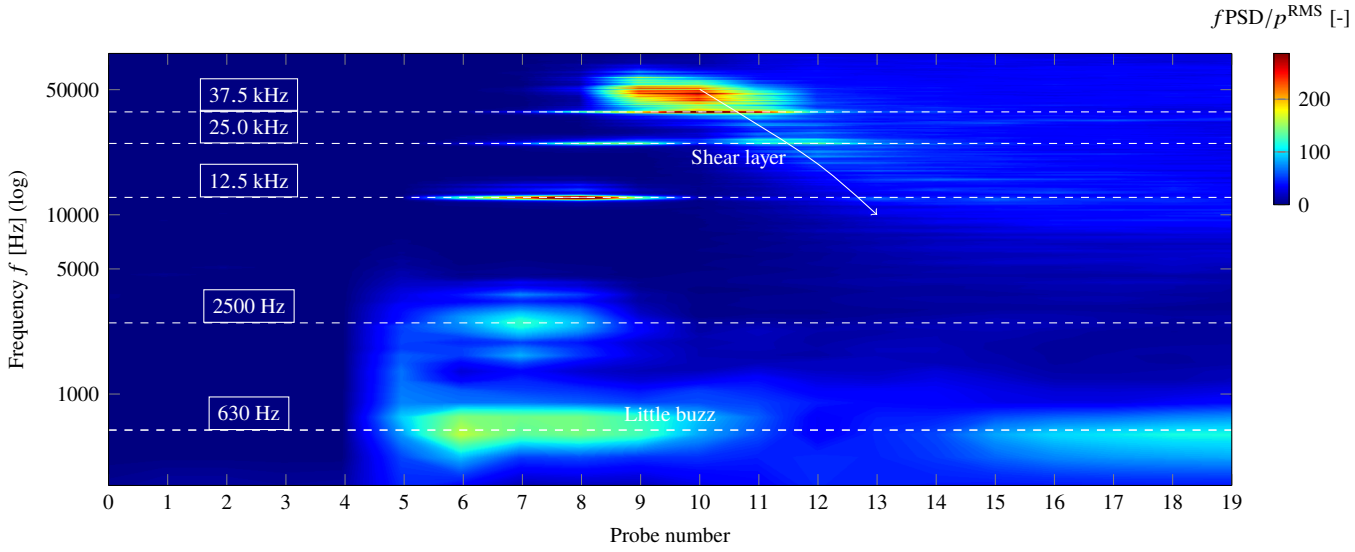

Figure 11 Spatio-frequential map of the pressure fluctuations along the longitudinal axis.

fluctuations in the median longitudinal plane. The pressure fluctuations are defined as the difference between the instantaneous pressure and the local time-averaged pressure:

$$\Delta p(t) = p(t) - \overline{p} \tag{12}$$

It is seen in Fig. 10 that positive and negative values of the fluctuating pressure are associated with the λ-shock ahead of the inlet entrance plane, indicating its oscillating motion. Farther downstream, the fluctuating pressure field features numerous regions of alternating positive and negative values (from the longitudinal position about $x = 0.03$ m). Those pressure fluctuations can be related to the developing shear layer between the separated area behind the diffuser ramp and the core flow in the channel. As they are convected downstream by the main flow, the fluctuating pressure pockets grow and eventually break down into smaller scale areas.

In order to link the frequency of the pressure fluctuations to their spatial localization, a spatio-frequential map is drawn in Fig. 11. This kind of representation allows for highlighting the spectral content of the pressure signal for different locations along the longitudinal axis. For probes 0 to 4, located ahead of the compression ramp, the flow is steady and there is no pressure fluctuation. From probe 5 to the most downstream one, the pressure exhibit non-zero fluctuations. For probes 5 to 9, it is seen that pressure fluctuations exhibit a peak at a frequency of 630 Hz, which has been related to the little buzz, and several narrow-band peaks at $f = 12.5$ kHz, $f = 25.0$ and $f = 37.5$ kHz which are multiple of each other. Their origin is still unclear but their narrow-band feature seems to indicate an acoustic origin. The spectral content of probes 5 to 9, is similar to that observed for the probe I and J in Fig. 9c excepted that around the probe 7 a slighter peak emerges at a frequency of 2500 Hz. Such a frequency has been found to be the main shock oscillation frequency for a higher throttling ratio (Fig. 9a). It thus seems that it is still present in the flow field for lower throttling ratio. In the case of the present throttling ratio, the value of the frequency is close to the fourth multiple ($630\,\mathrm{Hz} \times 4 = 2520\,\mathrm{Hz}$) of the little buzz frequency.

Between probe 10 and 15, there is a marked increase in the energy at high frequency (50000 Hz), with a tendency for the energy to spread from the highest frequency to the lower ones as we progress in the downstream direction (highlighted by an arrow in Fig. 11). This energy content may be associated with the shear layer which exhibits resolved turbulent structures from about the location of probe 10, as can be seen in Figs. 6 (numerical Schlieren field), 9c (Mach number field in the inset) and 10 (fluctuating pressure field). An empirical formula, proposed by Huerre [20], allows to estimate the frequency associated with a Kelvin-Helmholtz type instability in a shear layer:

$$f_{K-H} = 0.135 \frac{u_{\max} - u_{\min}}{\delta_\omega} \tag{13}$$

with $u_{\max}$ and $u_{\min}$ the mean flow velocity on both side of the shear layer and $\delta_\omega$its vorticity thickness. From the mean velocity profile accross the channel at the location corresponding to probe 10, the estimated frequency f_{K-H} is

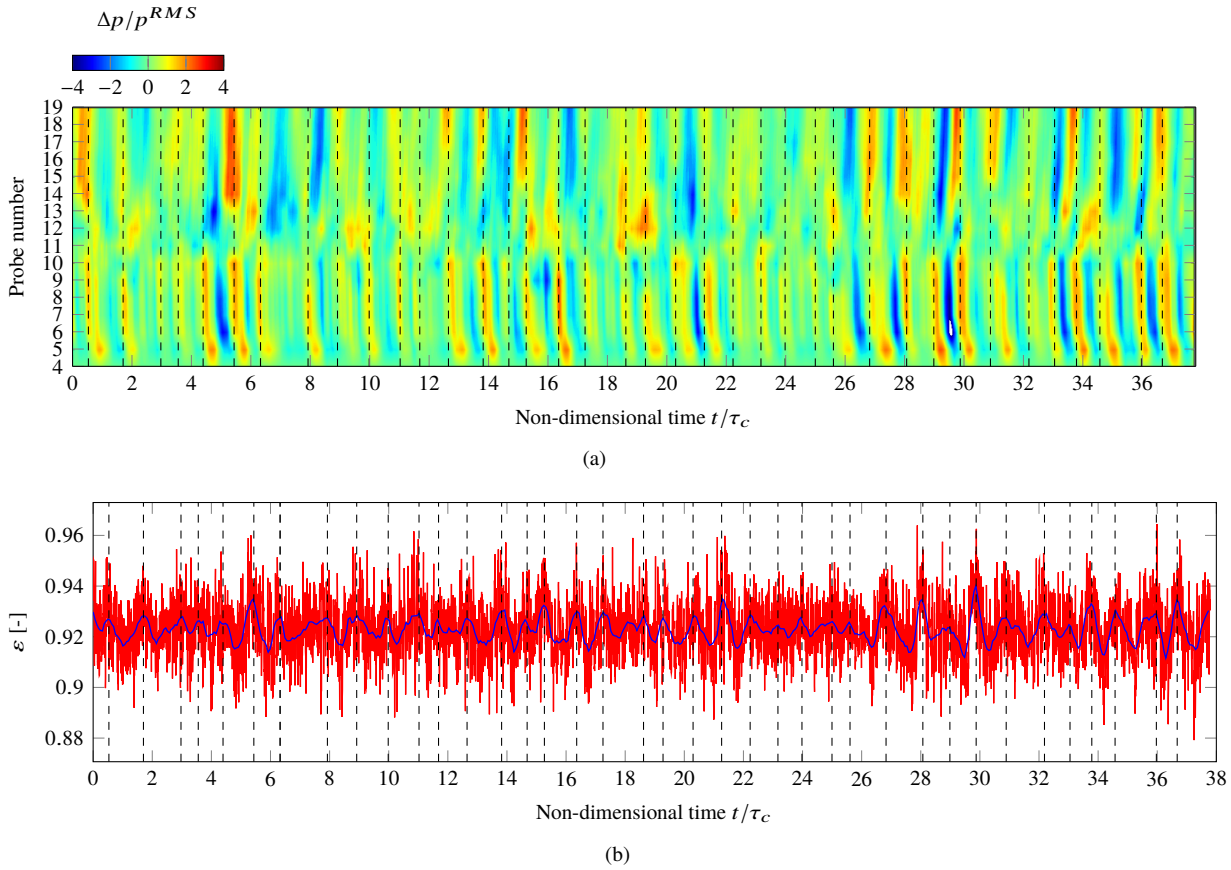

Figure 12 (a) Spatio-temporal map of the normalized low-pass-filtered pressure fluctuations $\widetilde{\Delta p}/p^{\mathrm{RMS}}$ along the longitudinal direction. (b) Time-evolution of the normalized mass flow ratio through the air inlet. (——) Unfiltered signal. (——) Low-pass filtered signal. (Vertical dashed lines) Instants associated with local maximal value of the normalized mass flow ratio.

45000 Hz, which is of the order of magnitude of the frequency at which turbulent energy is produced at the beginning of the shear layer, as shown in Fig. 11 for probe 10.

For probe 14 to 19, the frequency associated with the little buzz is the single one to clearly emerge from the spectrum. The little buzz can then be characterized as a global mode inasmuch as its related frequency emerges for most of the probes in the air inlet.

In order to highlight its spatial structure, a spatio-temporal map of the pressure fluctuations Δp normalized by the local root-mean-squared pressure p^{RMS} is drawn in Fig. 12a. Time has been nondimensionalized by the characteristic time of a little buzz period $\tau_c = 1/f$. The pressure signals have been filtered by means of the Savitzky-Golay filter [21] in order to remove the pressure fluctuations due to shear layer and other high-frequency phenomena. The cut-off frequency is 2000 Hz. The effect of the filter application can be assessed in Fig. 12b, which displays the time-evolution of the normalized mass flow ratio through the air inlet for both the unfiltered and filtered signal. The filtered signal clearly features a periodical variation of the mass flow ratio at the little buzz frequency. In Fig. 12a, it can been seen that the pressure varies periodically in the channel. Two distinct regions clearly exhibit such variations: the one between probe 5 and 10 and the other one between probe 12 and 19. The vertical dashed lines drawn in Fig. 12 mark the instants corresponding to peak value of the mass flow ratio. A close-up on several repetition of the periodic mode is displayed in Fig. 14a. It can be seen that the max-flow ratio instants generally correspond to a positive pressure fluctuation between probe 6 and 10 (fore part) and between probe 12 and 19 (rear part). When paying deeper attention to Figs. 12a and 14a, it seems that the pressure increase in the rear part of the channel occurs before the pressure rise in the fore part of the duct. Fig. 14a also shows that the instant at which pressure fluctuations is the highest in the rear part of the duct corresponds to a (slightly) negative pressure fluctuation at probe 5, near the oscillating shock. These observations

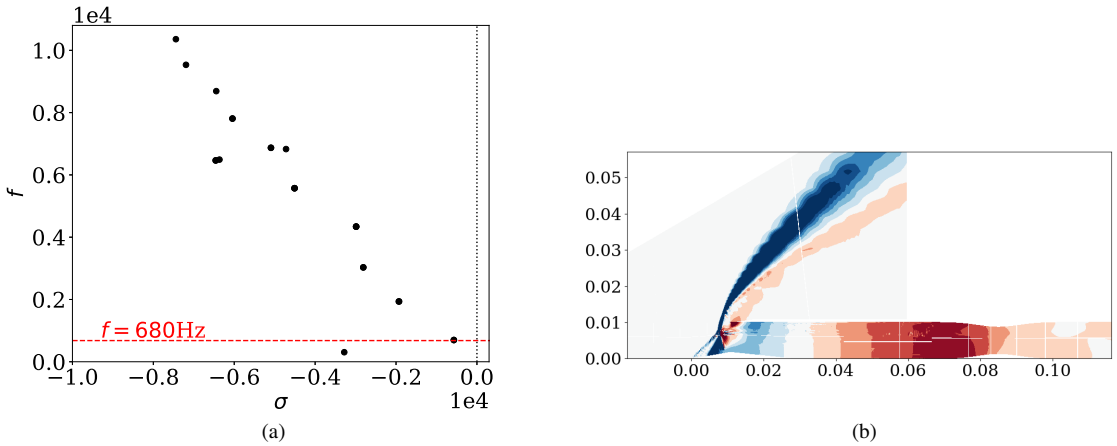

Figure 13 (a) Eigenspectrum of the Jacobian operator associated to the RANS equations, linearized about the steady RANS flow field with TR = 0.74. For each eigenvalue, its real part corresponds to the growth rate σ of the corresponding mode, while the imaginary part gives its frequency f. The red dashed line highlights the frequency of the mode corresponding to the buzz phenomenon. (b) Spatial structure of the pressure fluctuations associated to the mode related to the buzz phenomenon (arbitrary amplitude). The colormap has been saturated such that the fluctuations within the channel could be seen (their amplitude is very small compared to those about the shocks).

indicate that the pressure does not feature a clear overall in-phase fluctuation mode as it would be expected for the $n = 0$ fundamental duct acoustic mode to which is generally related the estimated frequency of buzz (equation 6). That may explain the discrepancies highlighted in Tab. 2 between the observed buzz frequencies and that estimated by eq. (6).

VI. Stability analysis

Unlike the good agreement between the URANS and ZDES simulations for TR associated with the big buzz phenomenon, the URANS simulations performed in the present work fail to reproduce any oscillations in the little buzz regime. Nonetheless, the following results show that the frequency of the little buzz phenomenon may still be accurately predicted from RANS results through a global stability analysis.

We focus on a RANS configuration associated with little buzz, with TR = 0.74. As explained in section IV, this flow field and the corresponding shock system pattern compares with a ZDES configuration with a higher throttling ratio: from Fig. 6, it best compares with the ZDES results with TR = 0.78, which exhibits fluctuations at a frequency $f = 630$ Hz. A global stability analysis then consists in computing a steady RANS field, and linearising the RANS equations about this field. For the present work, the corresponding linear operator $\mathcal{A}$, the so-called Jacobian of the system, is explicitly computed by finite differences, following the numerical strategy defined in [22]. Then, the computation of the eigenspectrum of this operator, shown in Fig. 13a, yields the set of linear global modes of the flow configuration (see for instance [22] for further details about the stability analysis procedure).

All eigenmodes are stable (growth rate $\sigma < 0$), which is consistent with the steady nature of the results obtained with the URANS simulation for this configuration. When focusing on the least stable mode, one may observe that it displays a frequency $f = 680$ Hz that is close to the results from the ZDES simulation, which indicates that this mode may indeed be related to the buzz phenomenon. The spatial structure of this mode, shown in Fig. 13b, confirms this assumption. Indeed, the mode displays the expected features of the little buzz phenomenon: the fluctuations involve the expected shock oscillations and, more interestingly, pressure waves propagating in the channel of the inlet. It may be observed that the fluctuations nearby the throat are out-of-phase with those nearby the shock, which is consistent with the observations from the ZDES results. A more thorough comparison between the ZDES simulation and stability analysis is performed in Fig. 14 where a reconstructed spatio-temporal map of 5 repetitions of the pressure mode associated with frequency $f = 680$ Hz is compared to the a close-up view of the spatial-temporal map shown in Fig. 12a. One can first notice the varying pressure in both the fore and rear part of the air inlet with a phase shift between each other. This shift is comparable to that observed for the ZDES simulation. Secondly, both ZDES and stability analysis

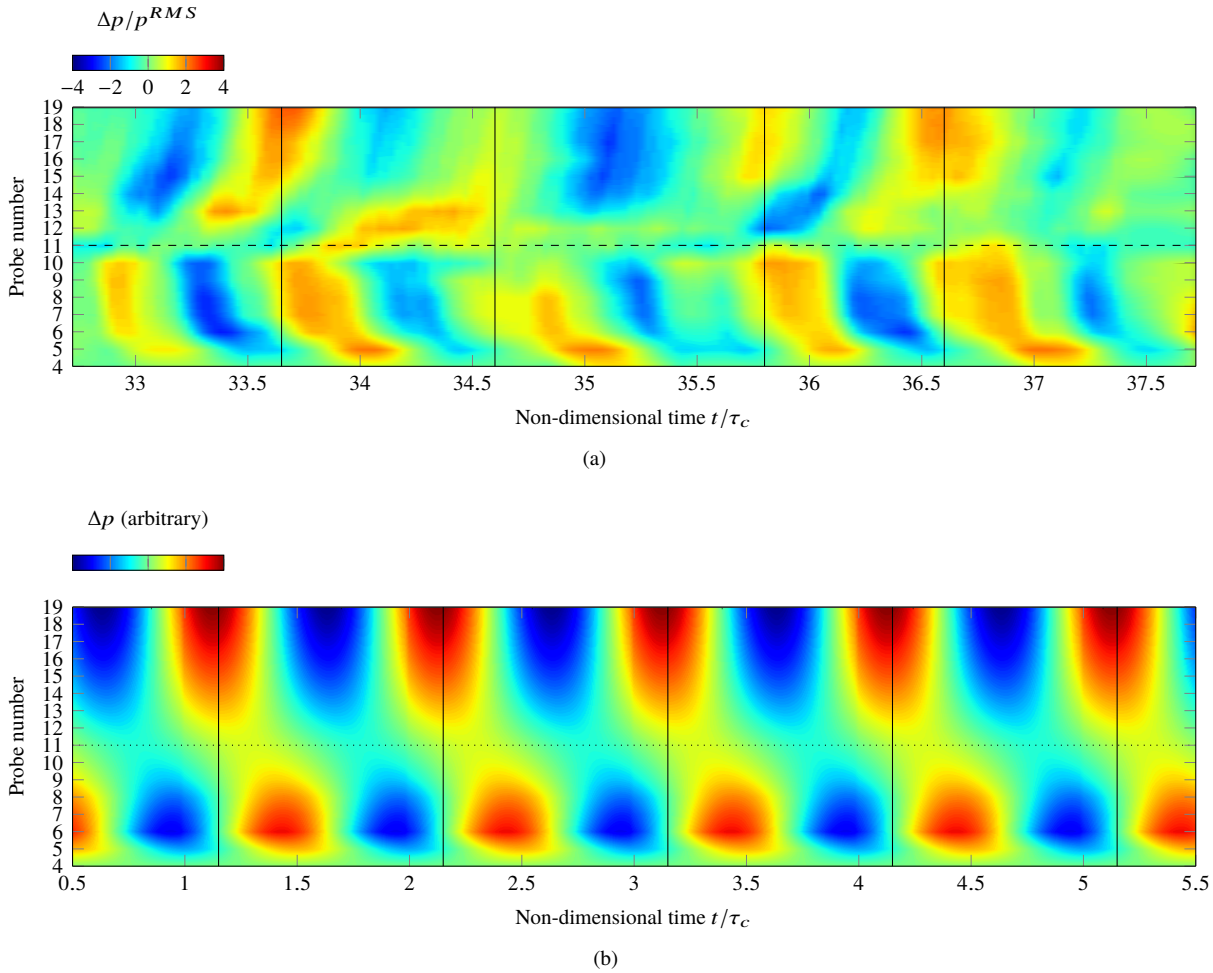

Figure 14 (a) Spatio-temporal map of the normalized low-pass-filtered pressure fluctuations $\widetilde{\Delta p}/p^{\mathrm{RMS}}$along the longitudinal direction from ZDES. (b) Reconstructed spatio-temporal map from the spatial mode associated with the least-stable frequency $f = 680\,\mathrm{Hz}$. . (Vertical solid lines) Instants corresponding to positive peak value of the pressure in the rear part of the duct.

seem to indicate that there is low intensity pressure fluctuations at the location of probe 11. This spatial form for the pressure mode is still unexplained. One can simply notice that the location of probe 11 corresponds to the end of the subsonic diffuser ramp which induces a sudden change in the duct cross-section evolution.

VII. Conclusions and Perspectives

In the present work, unsteady RANS and ZDES simulations have been carried out on a reduced model of an external compression supersonic inlet which exhibits shock oscillations when mass flow ratio decreases below a particular threshold. The results showed that both URANS and ZDES are able to reproduce the big buzz phenomenon which is associated to large amplitude shock oscillations. Furthermore, only the ZDES strategy have permitted to retrieve small amplitude shock oscillations referred as little buzz and occurring for higher mass flow ratio. For such cases, URANS simulations quickly converged to a steady-state. ZDES has been proven to be valuable tool for a deeper understanding of both little and big buzz phenomena. In particular, the unexplained shift between little buzz and big buzz frequency is well reproduced by this strategy. A detailed analysis of the pressure fluctuations has been carried out for a given little-buzzed configuration. Comparison with big-buzzed and less throttled configurations, which have also be computed by ZDES simulations, is still ongoing work in order to explain the frequency shift.

Eventually, preliminary results from a stability analysis of a little-buzzed configuration showed that the buzz

phenomenon is associated with a global mode of the linearized RANS operator, which opens the way to future studies and potential interesting insights regarding the buzz phenomenon. Future work will be dedicated to performing a large-eddy simulation (LES) of the reduced model in order to validate more quantitatively the ZDES simulations.

VIII. Acknowledgments

This work has been funded by the Onera research project PR-OPOSSUM dedicated to the prevision and control of supersonic air inlets. The author would like to thank E. Garnier and J. Dandois for their insightful advice. Special thank are due to P. Duveau and J.-M. Massonnat who provided the experimental data. The author is thankful to I. Mary for his technical support with the solver FastS.

References

[1] Ferri, A., and Nucci, L. M., "The Origin of Aerodynamic Instability of Supersonic Inlets at Subcritical Conditions," Tech. Rep. NACA RM-L50K30, 1951.

[2] Dailey, C. L., "Supersonic Diffuser Instability," *Journal of the Aeronautical Sciences*, Vol. 22, No. 11, 1955, pp. 733–749.

[3] Fisher, S., Neale, M., and Brooks, A., "On the sub-critical stability of variable ramp intakes at mach numbers around 2," Tech. Rep. ARC-R/M-3711, National Gas Turbine Establishment, 1970.

[4] Trapier, S., Duveau, P., and Deck, S., "Experimental Study of Supersonic Inlet Buzz," *AIAA Journal*, Vol. 44, No. 10, 2006, pp. 2354–2365.

[5] Newsome, R. W., "Numerical Simulation of Near-Critical and Unsteady, Subcritical Inlet Flow," *AIAA Journal*, Vol. 22, No. 10, 1984, pp. 1375–1379.

[6] Soltani, M. R., and Sepahi-Younsi, J., "Buzz Cycle Description in an Axisymmetric Mixed-Compression Air Intake," *AIAA Journal*, Vol. 54, No. 3, 2016, pp. 1040–1053.

[7] Lu, P.-J., and Jain, L.-T., "Numerical Investigation of Inlet Buzz Flow," *Journal of Propulsion and Power*, Vol. 14, No. 1, 1998, pp. 90–100.

[8] Kwak, E., and Lee, S., "Convergence Study of Inlet Buzz Frequency with Computational Parameters," *29th AIAA Applied Aerodynamics Conference*, 2011.

[9] Hong, W., and Kim, C., "Computational Study on Hysteretic Inlet Buzz Characteristics Under Varying Mass Flow Conditions," *AIAA Journal*, Vol. 52, No. 7, 2014, pp. 1357–1373.

[10] Trapier, S., Deck, S., and Duveau, P., "Delayed Detached-Eddy Simulation and Analysis of Supersonic Inlet Buzz," *AIAA Journal*, Vol. 46, No. 1, 2008, pp. 118–131.

[11] Lyubimov, D. A., and Potekhina, I. V., "A study of unsteady-state operating conditions of a supersonic inlet by the RANS/ILES method," *High Temperature*, Vol. 54, No. 5, 2016, pp. 737–744.

[12] Candon, S., Loth, E., Rybalko, M., and Hirt, S., "Acoustically Induced Shock Oscillations in a Low-Boom Inlet," *AIAA Journal*, Vol. 54, No. 7, 2016, pp. 2134–2148.

[13] Peron, S., Renaud, T., Mary, I., Benoit, C., and Terracol, M., "An Immersed Boundary Method for preliminary design aerodynamic studies of complex configurations," *23rd AIAA Computational Fluid Dynamics Conference*, 2017.

[14] Spalart, P., and Allmaras, S., "A one-equation turbulence model for aerodynamic flows," *30th Aerospace Sciences Meeting and Exhibit*, 2000.

[15] Spalart, P., "Trends in turbulence treatments," *Fluids 2000 Conference and Exhibit*, 1992.

[16] Deck, S., "Recent improvements in the Zonal Detached Eddy Simulation (ZDES) formulation," *Theoretical and Computational Fluid Dynamics*, Vol. 26, No. 6, 2012, pp. 523–550.

[17] Verrière, J., Gand, F., and Deck, S., "Zonal Detached-Eddy Simulations of a Dual-Stream Jet," *AIAA Journal*, Vol. 54, No. 10, 2016, pp. 3176–3190.

[18] Deck, S., "Zonal-Detached-Eddy Simulation of the Flow Around a High-Lift Configuration," *AIAA Journal*, Vol. 43, No. 11, 2005, pp. 2372–2384.

[19] Mary, I., and Sagaut, P., "Large Eddy Simulation of Flow Around an Airfoil Near Stall," *AIAA Journal*, Vol. 40, No. 6, 2002, pp. 1139–1145.

[20] Huerre, P., and Rossi, M., *Hydrodynamic instabilities in open flows*, Collection Alea-Saclay: Monographs and Texts in Statistical Physics, Cambridge University Press, 1998, p. 81–294. doi:10.1017/CBO9780511524608.004.

[21] Savitzky, A., and Golay, M. J., "Smoothing and differentiation of data by simplified least squares procedures." *Analytical chemistry*, Vol. 36, No. 8, 1964, pp. 1627–1639.

[22] Beneddine, S., "Characterization of unsteady flow behavior by linear stability analysis," Ph.D. thesis, Université Paris-Saclay, 2017.